Paper Title*

Isaac Sacramento
Department of Informatic and Statistics
Federal University of Santa Catarina
Florianpolis, Brazil
isaac.sacramento@posgrad.ufsc.br

Mauro Roisenberg
dept. name of organization (of Aff.)
name of organization (of Aff.)
Florianpolis, Brazil
email address

Rodrigo Exterkoetter
Departament of Computer Science
Federal University of Santa Catarina
Florianpolis, Brazil
email address

Leando P. de Figueiredo
Departament of Physics)
Federal University of Santa Catarina
Florianpolis, Brazil
email address

5th Given Name Surname
dept. name of organization (of Aff.)
name of organization (of Aff.)
City, Country
email address

6th Given Name Surname
dept. name of organization (of Aff.)
name of organization (of Aff.)
City, Country
email address

Abstract—**This document is a model and instructions for LaTeX. This and the IEEEtran.cls file define the components of your paper [title, text, heads, etc.]. *CRITICAL: Do Not Use Symbols, Special Characters, Footnotes, or Math in Paper Title or Abstract.**

Index Terms—**component, formatting, style, styling, insert**

I. Introduction

Deblurring is the task of estimating a sharp latent image, given a blurry image as input. According to [1], it is not observable in the literature an algorithm for deblurring all objects, i.e., domain-specific knowledge should, somehow, be incorporated to the algorithm in order to proceed effective deblurring. In oil exploration field, the seismic data acquisition and its inversion to acoustic impedance attribute typically generates blurry images of the subsurface, in such a way that it is not clearly observable the interfaces between different rock layers, the geological structures that make up the reservoir, such as channels, fans, traps, fails, connectivity patterns, etc. Obtaining high resolution acoustic impedance images, through seismic inversion methods, is a critical part in oil reservoir characterization. Despite the notorious efficiency of inversion methods, post-inversion images deblurring has not received much attention.

Reservoir characterization aims to determine a multidimensional structure and properties of an oil field. To achieve this goal, it is essential to combine, through an inversion algorithm, the informations, knowledges and available data about the field, in such a way that it is possible to make the quantitative predictions about the reservoir behavior [2]. Using the seismic data in deep-water reservoir modeling leads to errors in estimating the reservoir properties, because such data do not allow the wide understanding of the field under study [33]. To succeed in seismic inversion, it is necessary to

include strategies to deal with multiple sources of uncertainties. Specifically, the limited band-width of the seismic data leads to a misinterpretation of the resulting acoustic impedance models. According to [3], improving the resolution of seismic inversion is possible by adding high frequency in acquisition and processing seismic data. However, the earth attenuation, high-frequency noise and other sources, cause the lack of high and low frequencies in seismic data. Thus, deblurring the acoustic impedance models, as a post-inversion refinement process, should lead to a more accurate interpretation of the impedance models.

We approach the acoustic impedance deblurring through a CNN model. CNN is a framework of deep learning which has been used in a wide sort of machine learning tasks. The availability of benchmarks [4] and the advances in Graphical Processing Unit (GPU) [5] allowed CNN to outperform state-of-the-art techniques in detection [6], [7], model-free tracking [8], classification [9]. With excellence in feature learning, CNN achieved notorious success in image and video classification [10], [11], action and speech recognition [12], [13]. Under the perspective of the reservoir characterization, CNN has been applied to lithofacies recognition [14] and calculation [15]. However, there is a lack of researches on improving the resolution of images resulting from inversion processes.

In this paper, we propose a new multilayer convolution network model to perform deblurring in post-inversion acoustic impedance. Each network layer maps higher level features originated in the previews layers through convolutional blur kernels. To perform this mapping, the kernels, also named weights, are adjusted by minimizing a loss function. The model enhances the resolution of acoustic impedance images, resulting in sharp images with increased high-frequency bandwidth and lower noise. In order to train the model, we blur a set of the synthetic acoustic impedance images to create a dictionary of images of high and low resolution. Then, the pairs of blur and latent images are normalized and pre-

sented to the network as input and target, respectively. In our approach, the domain-specific knowledge used in deblurring acoustic impedance impedance images is comonly obtained through training images containing geological knowledge. Generally, the images are obtained from a specialist (geologist or geophysicist) knowladge about relevant characteristics of the reservoir for which one wishes enhancing the impedance images. The core concept of our architecture is the combination of the convolution layers with regression layers, thus the convolutional layers learn the spatial structures existing in different acoustic impedance images, while the regression layer proceed the prediction of the property values.

II. THEORETICAL FOUNDATIONS AND RELATED WORKS

Inversion theory is used in several areas to infer parameters values related to physical processes based on experimental data. Inversion modeling refers to using the current measurements of observable physical parameters in order to infer the current model parameters (not observable). The inversion problem is described as (1)

$$m = F^{-1}(d) \tag{1}$$

where, F is the investigated physical system, and relates a set of model parameters $m = (m_1, m_2, ..., m_n) \subset R^n$ estimated through the observed data $d \in R^s$. Geophysical methods frequently involve the solution and assessment of inversion problems. Studying these problems allow inferring physical properties distributions in the earth subsurface, using measured data. Among these data, the seismic data is mainly used in seismic inversion, which plays an important role in reservoir characterization. From a practical perspective, solving seismic inversion problems improves the exploration and management in oil industry, once the seismic data is highly correlated to petrophysical properties, e.g., density and porosity in subsurface.

The offshore seismic data is the main observable data used in seismic inversion. To perform seismic acquisition, one sends pulses through a controlled artificial source and captures the vertical component responses in function of time. The seismic data is a composition of the wave pulse used in the acquisition, named wavelet, and the characteristic of the interfaces between rock layers, on which the wavelet reflects. This rock layer characteristic is called reflectivity coefficient and it is calculated as (2)

$$r(t) = \frac{z(t + \delta t) - z(t)}{z(t + \delta t) + z(t)}, \tag{2}$$

where, $z(t)$ is the acoustic impedance, in function of time t, defined as $z(t) = \rho(t)v(t)$, where $\rho(t)$ is the rock density and $v(t)$ the propagation velocity of acoustic wave. Therefore, the seismic data $d(t)$ is modeled as a discrete convolution operation $*$ of the wavelet s with the reflectivity coefficient r as (3)

$$d(t) = s(\tau) * \sum_{j-1}^{N} r(t - t_j)\delta(t - t_j) + e_d(t) \tag{3}$$

where, N is the number of subsurface layers, $e_d(t)$ is a random noise in function of time. One ideal wavelet is a delta pulse with complete frequency band-width, however, in practice wavelets have their band-width generally limited from $6Hz$ to $65Hz$. By consequence, the images resulting from the seismic inversion will keep their frequency spectrum limited.

According to [16], a good acoustic impedance model contains more information than the seismic data, because the inversion process contains additional information originated from well-logs, for exemple, a low-frequency model. The well-logs are real data measured in wells spread along the field. With the local acoustic impedance it is possible to calculate the low-frequency model by interpolation between wells [17], [18]. Despite of the low-frequency model, the final model for acoustic impedance still lacks of high resolution details.

Deblurring is generally modeled as the convolution of a blur kernel k with a latent image I:

$$y = k \otimes I + n \tag{4}$$

where n is the noise. Since k, I and n are unknown, the problem is highly ill-posed and admits infinite solutions for k and I. Several works have developed different deblurring methods for specific purposes. Blind deconvolution methods are widely investigated in image processing [19]. For the last six years, considerable effort has been made in single image [20]–[23] and multi-image [24], [25] blind deconvolutions. Applying blind deconvolution generally implies in making assumptions on blur kernels and/or on latent images. For example, assuming sparsity of blur kernel or that natural images have super-Gaussian statistics. The second assumption leads to the use of image priors on inference process and, consequently, to the maximum *a posteriori* (MAP) estimation [20]. However, [26] show that deblurring methods based on this prior tend to favor blurry images over original latent images.

The Bayesian inference approach [26] outperforms the MAP based methods. It marginalizes the image from the optimization step, while estimating the unknown blur. The authors show that it is possible to define a class of prior image based on natural image statistics, suitable enough to represent sharp images features. This prior formulation makes possible to use Bayesian inference in the estimation of the unknown image and the blur kernel. According to [27], defining a gradient prior, by itself, is not sufficient to reach a sharp image, instead, they search in a dataset for a prior that densely correspond to the blurry image similar to a sharp image. This search is an iteratively optimization over the correspondence between the images, the kernel and the sharp image estimation. Even though [28] suggest a generalization for the method proposed by [27], it still requires a similar reference image, which is not always available.

The optimization methods previously described use a set of priors based on generic image statistics or domain-specific priors. It has been demonstrated that these methods work properly on synthetic blurs. However, new studies show that they failure when applied to real world blurry images [29] and
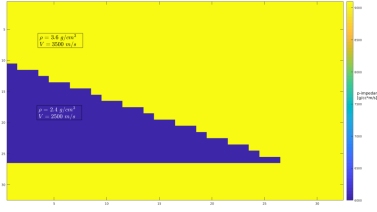
Fig. 1. Acoustic impedance model generation. Wedge with reference values for density and compressional velocity.
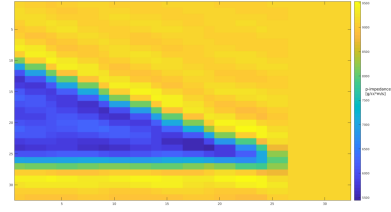

Fig. 2. Acoustic impedance blurred model.

take a severe computational cost [30]. In contrast, the learning-based methods have gained attention with the resumption and recent advances in convolutional neural networks (CNN). The adequate hyper-parameter adjustment allows CNN to learn non-linear function or blur kernels. Thus, deblurring becomes a function of a blurry image I and a set of parameters p as (5)

$$y = \sigma(I, p) \qquad (5)$$

Learning-based methods focus on developing a model to learn the function σ [31] and to perform non-blind deblurring [30]. [32] teaches a CNN to recognize motion kernels and performs non-blind deconvolution in dense motion field estimate, in addition, [31] minimize regularized l_2 in order to perform text deblurring.

III. Data and Methods

A. Acoustic Impedance Inversion

The experiments described in this paper perform on a set of synthetic acoustic impedance images. Using synthetic models to test and parametrize algorithms is a common practice in reservoir characterization [33]. It allows studying the results of the algorithms without external interferences and performing efficient interpretations and assessments. According to [34], wedge shaped models is a straight way to analysis the seismic model and inversion processes. It reproduces reservoir contexts such as stratigraphic refinements, edges and channel structures in a realistic manner.

The training set generation occurs in two steps. The fist step creates a set of wedge shapes represented by images with size 32 x 32. The wedge shapes represent the reservoir and they randomly vary in width and length. The second step fills the lithology with values of petrophysical properties. In order to simplify the assessments and conclusions, we fill the lithology structures with constant reference values of rock densities and compressional velocity observed in the literature [35]. The acoustic impedance is calculated using the density and velocity models and the images in high resolution model are obtained, as illustrated in Fig. 1.

In a real scenario, the blurry acoustic impedance is the result of an acoustic inversion method, such as Maximum *a posteriori* [17], [18], Sparse Spike [36] and Recursive Inversion [37], using seismic data with limited band-with. However, for experimental purpose, the acoustic impedance models were filtered and the high frequencies were removed to obtain the

blurry images, as illustrated in Fig. 2. This way, the supervised learning is performed with the high resolution images and blurred images. To increase the number of examples in the training dataset we rotate the impedance models to establish the wedge structure in four different angles ($0°$, $90°$, $180°$ and $270°$). This approach allows the model learning an wide edge variabilities in wedges images.

B. Proposed Architecture

The workflow of the proposed method consists of the following steps:

- Generate the synthetic impedance images;
- Blur the images through a low-pass filter;
- Train the convolutional model with the pair of high and low resolution images;
- Test the model with different blurry images;
- Assess the result for the testing output.

The CNN is a well established method for pattern recognition and image classification. Thus, an important breakthrough when applying CNN to deal with physical property images is developing a model capable to solve regression tasks. The model presented in this paper is able to solve two important problems related to deblurring images of physical properties : (1) learning the spacial patterns in the low resolution training images and (2) predicting each pixel intensity value in the new higher resolution image. To reach these two goals, our model, outlined in Fig. 3, comprises two major components that are combined to perform deblurring and physical property prediction jointly: (1) convolutional component and (2) regression component. The convolutional component is a two layer structure that maps a blurry image to a non-blurred model, while the regression layer is supposed to predict the continuous values of each pixel representing the acoustic impedance value. The state-of-the-art CNN models for image deblurring [1] and super-resolution [38] classify each pixel in the input image. Using these methods to solve the issue of deblurring continuous physical properties implies in discretization of each pixel in order to generate an image file. However, returning to the original data, results in information loss, what represents a serious inconvenient. Thus, combining the convolutional approach with the regression layer to deblur and predict the physics property represents a relevant advance.

C. Implementation Details

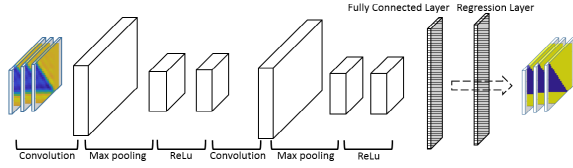The model is implemented using the Deep Learning toolbox delivered in MATLAB R2017A. Our model comprises a

Fig. 3. Proposed model achitecture.

simple architecture with two convolutional layers. Each one of them is configured with 50 kernels, sized 5 x 5 and stride 1, meaning that after each convolution operation the blur kernel is shifted one position in each direction. After each convolutional layer we proceed a maximum pooling operation to obtain the maximum value of small regions in the input image and obtain statistical summaries of these regions. We also apply rectified linear units (ReLU) after each pooling layer in order to speed up the training step and to learn sensible features from the images, following the proposal of [39]. After the second regularization layer, we add a fully connected layer, which maps the convolution layer's output to 1024 neurons. Finally, the output layer comprises a regression unit to predict the intensity of acoustic impedance in each pixel. The output vector is then resized to the original image dimension.

For training the network, we use a mini-batch with size of 32 training examples and we adopt an exponentially decreasing learning rate (initially set to 0.005), decreasing every iteration in a total of 100 iterations. It should be noted that, once the wedge shapes are randomly generated, every image is different and each one is introduced only once to the network, this way avoiding over-fitting. The network weights initialize randomly and the model performs a supervised learning through a dictionary containing pairs of low resolution and high resolution images. The Stochastic Gradient Descent with Momentum (SGDM) [40] adjusts the network weights in every layer by minimizing the Mean Squared Error (MSE) in each batch of images. Thus, after the training phase, the model is capable to deblur any other wedge shaped acoustic impedance image not presented in the training dataset. The output image recovers the high frequencies and shows higher similarity to the high resolution image than to the blurred image, according to established metric. The model is adjusted to deblur a wide variety of wedge shapes and impedance values. Thus, the images whose wedges the model are unable to predict, are used to form a new training dataset and the model is retrained. Three metrics assess the performance of our convolution network: Fast Fourier Transform Index - FFTI (6), Rooted Mean Square Error - RMSE (7). The FFTI is a similarity metric calculated based on the fast fourier transform (FFT) of each image. It is introduced by [41] and calculates as

$$C = \frac{(\sum_{i=1}^{N} F_{1i} F_{2i} - N \bar{F}_1 \bar{F}_2)^2}{(\sum_{i=1}^{N} |F_{1i}|^2 - N \bar{F}_1^2)(\sum_{i=1}^{N} |F_{2i}|^2 - N \bar{F}_2^2)}, \quad (6)$$

where, for each frequency, an intensity value is calculated from the real and complex parts of the fourier transform. F_{1i} represents the intensity value of i-th *pixel* in the first image

and F_{2i} is the intensity value of i-th *pixel* in the second image. $\bar{F}_1$ e $\bar{F}_2$ are the mean frequencies in each image. The closer FFTI is to 1, the higher the similarity between images. Additionally, we use the frequency spectrum to show the graphics of magnitudes, which allow distinguishing what high frequencies are added to the acoustic impedance after the low resolution images pass through the trained CNN.

$$RMSE = \sqrt{\frac{(\sum_{i=1}^{N} (x_i - y_i)^2)}{N}}, \quad (7)$$

IV. EXPERIMENTS

To build the training dataset we generate 500 images of random wedge. Because the last layer of the network is a regression unit, it is necessary the normalization of the images to values between 0 and 1, and the results are presented in terms of this normalization. The normalized images are then rotated according to the established angles mentioned in Section III, then comprising a total of 2000 images. By doing so, we present to the network the same lithologies in different positions and expect that the network identify general sorts of wedges in different angles. The rotated images are blurred by applying a low-pass filter with $4Hz$ cutting frequency, then the pairs of blurred and not-blurred images are used to adjust the model weights. It is relevant to mention that the images which are blurred with the same cutting frequency and that remain symmetric after the rotation, what means that rotating the images causes no changes in impedance values.

In the following subsections we present the results divided into the cases we consider relevant to test. First, we test the wedges rotated according to the established angles and with acoustic impedance values normalized to 0 and 1. Next, we test images with impedance values normalized to the interval between 0.3 and 0.7, therefore, out of the range used during the training phase. We then assess the model response to images blurred with different cutting frequencies. At last, we present to the model wedges with random shapes, rotated at random angles.

A. Integer Angles Rotated Wedges

We firstly test the network capability to correctly model the shape of wedges and to deblur their edges and contours in a simple perspective. Thus, the training and test images have the same reference values for density and compression velocity, different from each other only by the shape. Comparing the blurry images in Fig. 4b and the CNN outputs in Fig. 4c, the CNN outputs notably reach sharp images and accurately predict the pixel intensities. Tab. I shows that the error values between the network output and the latent images are considerably lower than the RMSE between the latent and the blurry images. Furthermore, the FFTI slightly increases and indicates more similarity between the network outputs and the latent images, except for the first image, for which the FFTI shows not representative change.

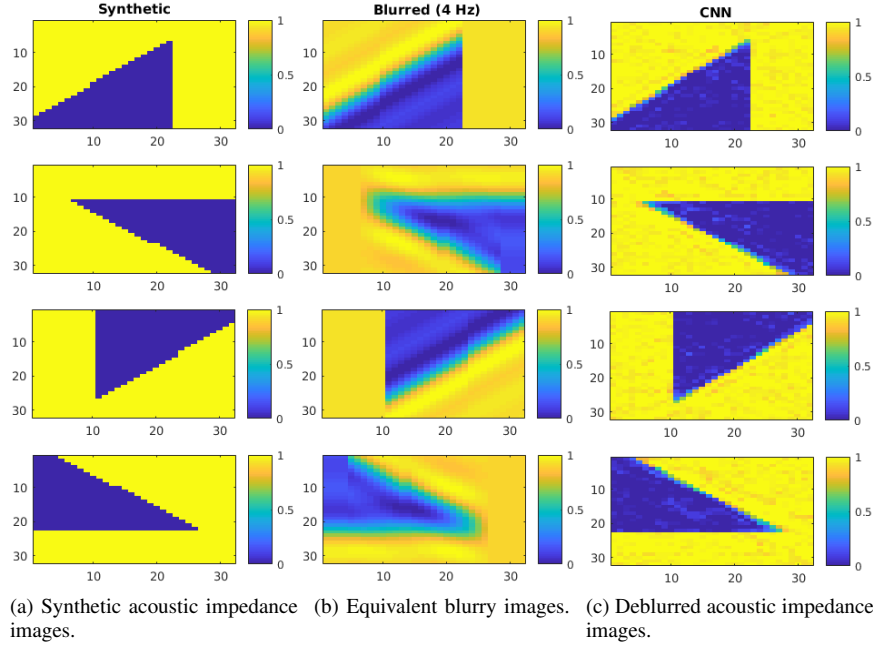In the following scenario, we arbitrarily change the normalized impedance in both lithologies to values 0.7 out of the

(a) Synthetic acoustic impedance images. (b) Equivalent blurry images. (c) Deblurred acoustic impedance images.

Fig. 4. First test case: the wedges are positioned in $0°$, $90°$, $180°$ and $270°$ and the acoustic impedance values are normalized to 0 and 1.

Metrics	Blurry Image (MSE - FFTI)	CNN (MSE - FFTI)
Example 1	0.1337 — 0.9773	0.0621 — 0.9724
Example 2	0.1972 — 0.9464	0.0776 — 0.9747
Example 3	0.1337 — 0.9773	0.0616 — 0.9861
Example 4	0.1976 — 0.9498	0.0767 — 0.9771

TABLE III
AN EXAMPLE OF A TABLE

	Blurry Image (MSE - FFTI)	CNN (MSE - FFTI)
Example 1 ($13Hz$)	0.0820 — 0.9963	0.0763 — 0.8094
Example 2 ($6Hz$)	0.1606 — 0.9780	0.1025 — 0.9886
Example 3 ($17Hz$)	0.0961 — 0.9966	0.0781 — 0.9921
Example 4 ($20Hz$)	0.1236 — 0.9938	0.1923 — 0.9810

TABLE II
AN EXAMPLE OF A TABLE

	Blurry Image (MSE - FFTI)	CNN (MSE - FFTI)
Example 1	0.0433 — 0.9830	0.0329 — 0.0988
Example 2	0.0605 — 0.9647	0.03677 — 0.9814
Example 3	0.0433 — 0.9830	0.0336 — 0.9801
Example 4	0.0605 — 0.9649	0.0374 — 0.9804

In a real data scenario, physical aspects, such as signal attenuation caused by the depth, lead to different blurring profiles in post-inversion images, what motivates this test case. In order to investigate this scenario, we blur each synthetic image with a different cutting frequency, randomly chosen between 3 and $20Hz$. Fig. 6 shows that the model deblur images containing different blurry resolution, and highlight edges and possible interfaces between rock layers. Metrics in Tab. III show that the RMSE of each CNN output is lower than the RMSE of the blurry images, even though its magnitude is considered non-representative.

B. Randomly Rotated Wedges

The randomly rotated wedges are related to lithologies positioned at random angles. In this case, we evaluate the CNN capability to deblur the wedges with specific shape and position, that are absent of the training dataset. We test the wedges with the acoustic impedance normalized to values equals to 0 and 1. It is observable in Fig. 7 that the model presents higher uncertainty in modeling the edges and corners of the wedges. On the other side, as the test images contain the same range of values as in the training images, the model keep its predictive capacity and recover the This result is evident
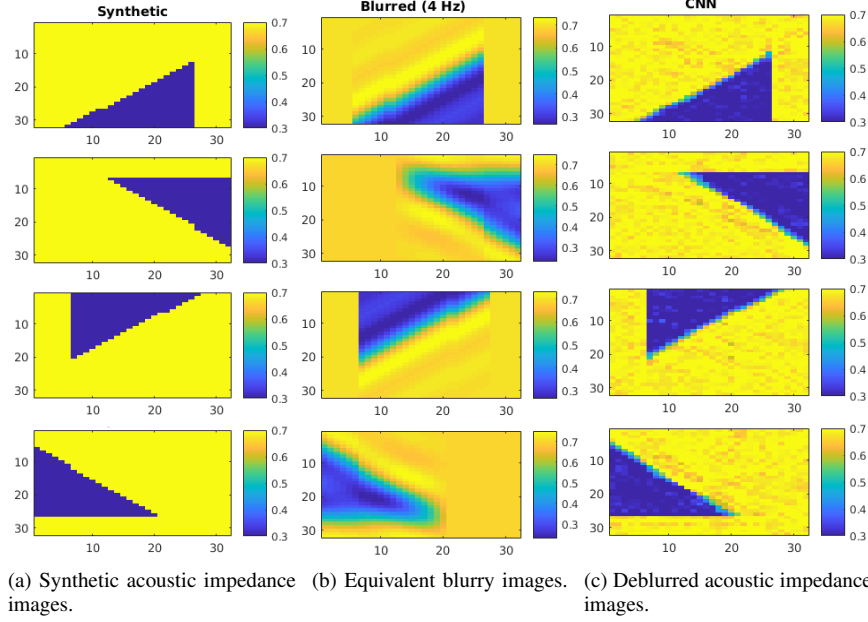
wedge and 0.3 into the wedge. These values are different from those learned at first by the model during the training phase and we test the model generalization capability to reach the learned pixel intensities. Once the model is trained with pixel valued to 0 and 1, it poorly extrapolated to the new values. Thus, we retrained the model with a new dataset containing 30% of images normalized to the mentioned impedance values $(0.7, 0.3)$ and tested with the images shown in Fig. 5b. It is noticeable in Fig. 5 that the network trained with the new dataset, learned the wedges shapes and the predicted pixel intensities, with low variance. Considering the CNN outputs, the metric values in Tab. II show that the RMSE slightly decrease, while the similarity with the latent image increases.

(a) Synthetic acoustic impedance images. (b) Equivalent blurry images. (c) Deblurred acoustic impedance images.

Fig. 5. The wedges are positioned in $0°$, $90°$, $180°$ and $270°$. The acoustic impedance values are normalized to 0.3 and 0.7.

(a) Synthetic acoustic impedance images. (b) Equivalent blurry images. (c) Deblurred acoustic impedance images.
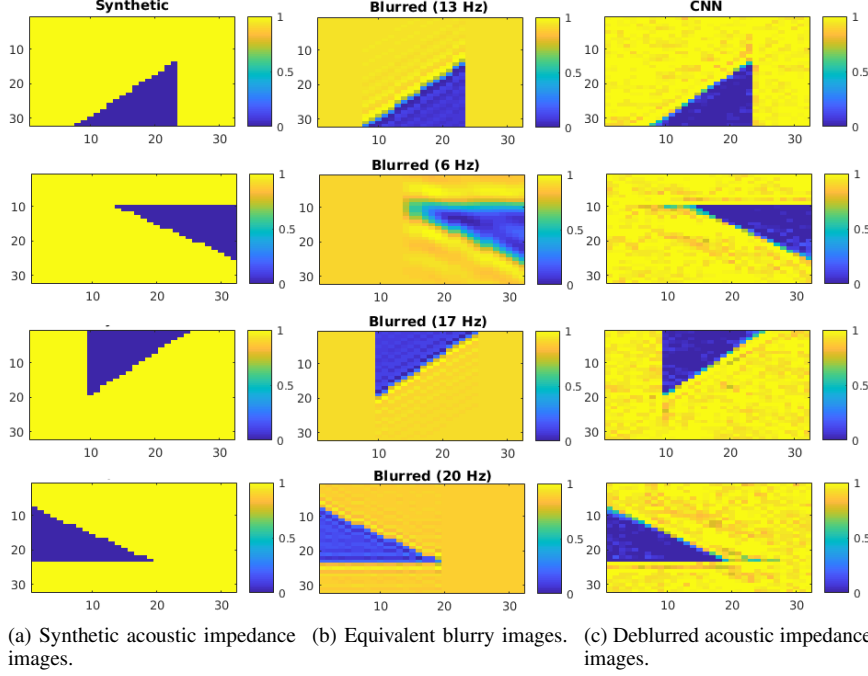
Fig. 6. The wedges are positioned in $0°$, $90°$, $180°$ and $270°$. The acoustic impedance models are blurred using different cutting frequencies.

in the metrics values (Tab. IV). In examples 2 and 4, the network outputs present lower RMSE than the blurry images, while it is higher in the other examples 1 and 3. However, according to the FFTI, all network outputs are less similar to the latent image, than the blurred image and we believe that is explained by the higher uncertainty observed. A mitigation for this problem is adding examples of this image to the network training dataset, as stated previously in Section IV-A.

C. Frequency Recovering

A relevant aspect of deblurring acoustic impedance images is the evidence of high frequencies recovering in the deblurry images and in the resulting seismic data. Here, we use the Fourier Transform to introduce the graphs containing frequency magnitudes of each image in our test examples.

The frequency magnitudes in our first test case, illustrated in Fig. 8a, show that the model precisely recovered the fre-
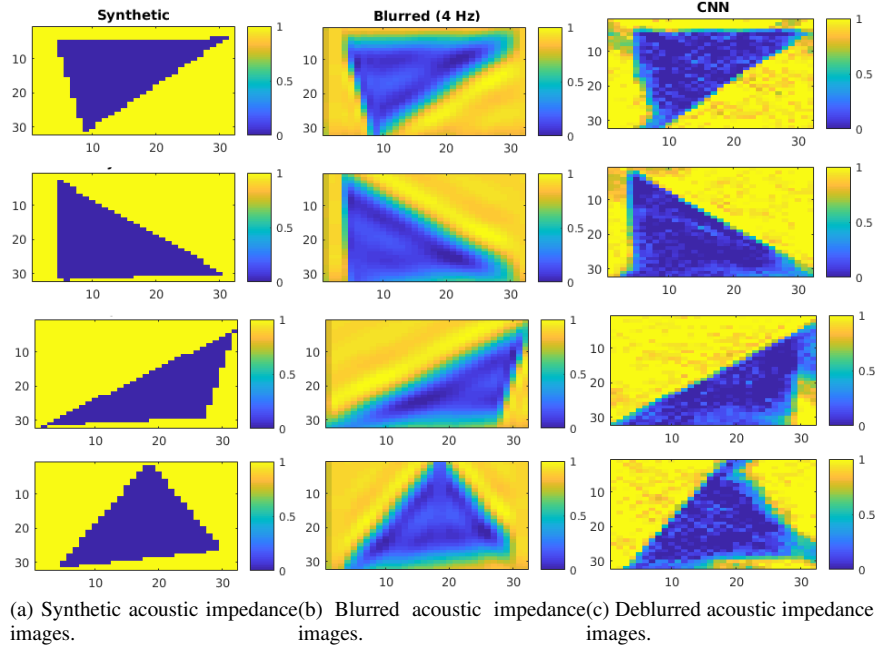
(a) Synthetic acoustic impedance images.   (b) Blurred acoustic impedance images.   (c) Deblurred acoustic impedance images.

Fig. 7. Examples in which the wedges have random shapes and are positioned at random angles.

	Blurry Image (MSE - FFTI)	CNN (MSE - FFTI)
Example 1	0.2283 — 0.9333	0.1959 — 0.9261
Example 2	0.2235 — 0.9309	0.2306 — 0.8974
Example 3	0.2319 — 0.9321	0.2681 — 0.9157
Example 4	0.2238 — 0.9348	0.2353 — 0.9067

quency spectrum of the original image. The resulting acoustic impedance shows increasing frequency magnitude in the range between $20Hz$ and $50Hz$, and between $60Hz$ and $100Hz$. This test case represents the ideal result due to the decreasing error, increasing similarity and frequency band-with in the CNN output images. Next, by training the model with the new dataset containing acoustic impedance images normalized to 0.3 and 0.7, we recovered the frequency magnitudes slightly lower than the ones of latent images, in the range of higher frequencies (Fig. 8b). This result reflects the insertion of only 30% images normalized to the mentioned range of property values. Figure 8c shows the recovering of frequency spectrum for images blurred with random cutting frequencies. Clearly, our model is able to deblur and highlight interfaces separating rock layers, for impedance images containing different blurs caused by attenuation elements in seismic data acquisition. Finally, for the test images with random shape and position, the proposed model recovered magnitudes higher than in the latent images (Fig. 8d). This result still depend on a new assessment due to the increase in frequency magnitudes between $10Hz$ and $60Hz$, whereas the metrics suggest higher error and lower similarity in the comparison among the model outputs and the blurry images.

V. Conclusion

In this paper, we introduce a convolutional neural network model for recovering high-quality synthetic acoustic impedance images from degraded images (blurry, noisy). Moreover, we introduce a simple architecture composed by a convolutional and a regression component. We demonstrate that, the proposed CNN recovers the high frequencies magnitudes, absent in blurry images. Experimental results validate the proposed method in different blurry scenarios. The methodology is promising for deblurrying acoustic impedance images, due to its capability in highlighting the edges and contours of wedge shaped lithologies and, in addition, predict the values of rock property. For future work, we aim to assess the model on real post-inversion acoustic impedance images and investigate its influence on seismic profile.

Acknowledgment

References

[1] G. G. Chrysos, and S. Zafeiriou, "Deep Face Deblurring." pp. 2015-2024, 10.1109/CVPRW.2017.252, 2017.

[2] JJM. Buiting, M. Bacon, "Using geophysical, geological, and petrophysical data to characterize reservoirs in the North Sea." in 5th Conference on Petroleum Geology of NW Europe, London. CD-ROM.

[3] X. Xiaoyu, L. Yun, S. Desheng, G. Xiangyu, and W. Huifeng, "Studying the effect of expanding low or high frequency on post-stack seismic inversion," in SEG Technical Program Expanded Abstracts 2012, pp. 1-5, September 2012.
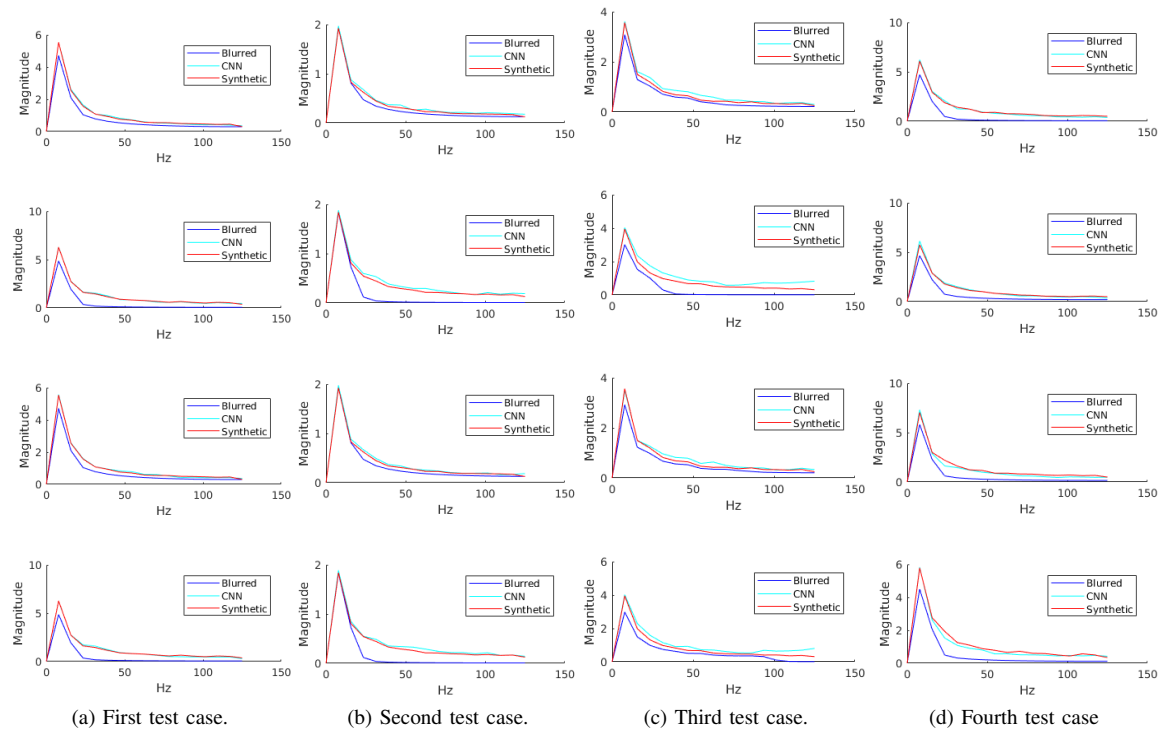
(a) First test case. (b) Second test case. (c) Third test case. (d) Fourth test case

Fig. 8. Frequency magnitude distributions.

[4] O. Russakovsky, J. Deng, H. Su, J. Krause, S. Satheesh, S. Ma, Z. Huang, A. Karpathy, A. Khosla, M. Bernstein, "Imagenet large scale visual recognition challenge," in ternational Journal of Computer Vision (IJCV), pp. 211252, 2015.

[5] N. Buduma, " Fundamentals of Deep Learning," Academic Press, in O'Reilly Media, 2015.

[6] R. Girshick, "Fast r-cnn," In IEEE Proceedings of International Conference on Computer Vision (ICCV), pp. 14401448, 2015.

[7] S. Bell, C. L. Zitnick, K. Bala, and R. Girshick, "Inside-outside net: Detecting objects in context with skip pooling and recurrent neural networks," in arXiv preprint arXiv:1512.04143, 2015.

[8] H. Nam and B. Han, "Learning multi-domain convolutional neural networks for visual tracking," In IEEE Proceedings of International Conference on Computer Vision and Pattern Recognition (CVPR) IEEE, 2016.

[9] K. He, X. Zhang, S. Ren, and J. Sun, "Deep residual learning for image recognition," In IEEE Proceedings of International Conference on Computer Vision and Pattern Recognition (CVPR). IEEE, 2016.

[10] A. Krizhevsky, I. Sutskever, G. E. Hinton, "Imagenet classification with deep convolutional neural networks: Advances in neural information processing systems," 2012, pp. 10971105.

[11] O. Abdel-Hamid, A.-r. Mohamed, H. Jiang, L. Deng, G. Penn, and D. Yu, "Convolutional neural networks for speech recognition," in IEEE/ACM Transactions on audio, speech, and language processing, num. 22, pp. 15331545, 2014.

[12] S. S. Farfade, M. J. Saberian, and L.-J. Li, 2015, "Multi-view face detection using deep convolutional neural networks," in Proceedings of the 5th ACM on International Conference on Multimedia Retrieval, ACM, pp. 643650.

[13] S. Ji, W. Xu, M. Yang, K. Yu, 2013, "3d convolutional neural networks for human action recognition," in IEEE transactions on pattern analysis and machine intelligence, num. 35, p. 221231.

[14] Q. Feng, Y. Miao, S. Ming-Jun, W. Yaojun, H. Guangmin, "Seismic facies recognition based on prestack data using deep convolutional autoencoder,".

[15] L. Lihui, L. Rong, L. Jianhai, Y. Wenkui, "Seismic Lithofacies Computation Method Based on Deep Learning," in International Geophysical Conference, pp. 649-652, April 2017.

[16] R. B. Latimer, R. Davidson, P. van Riel, "An interpreter's guide to understanding and working with seismic-derived acoustic impedance data," in The Leading Edge, pp. 242-256, vol. 19, num. 3, 2017.

[17] A. Buland, and H. Omre, "Bayesian linearized avo inversion," In Geophysics, 2003, pp. 185198.

[18] L. P. Figueiredo, M. Santos, M. Roisenberg, G. Neto, and W. Figueiredo, "Bayesian framework to wavelet estimation and linearized acoustic inversion," in Geoscience and Remote Sensing Letters, pp. 15, 2012.

[19] T.E. Bishop, S.D. Babacan, Amizic, T. Chan, R. Molina, and A. Katsaggelos, "Blind image deconvolution: problem formulation and existing approaches." in. Blindimage deconvolution: theory and applications, CRC press, 2007.

[20] S. D. Babacan, R. Molina, M. N. Do, and A. K. Katsaggelos, "Bayesian blind deconvolution with general sparse image priors." in Proceedings of European Conference on Computer Vision (ECCV), pp. 341355, 2012.

[21] D. Krishnan, T. Tay, and R. Fergus, "Blind deconvolution using anormalized sparsity measure." In CVPR, 2011.

[22] A. Levin, Y. Weiss, F. Durand, and W. T. Freeman. "Efficient marginal likelihood optimization in blind deconvolution." In CVPR, 2011.

[23] H. Zhang, J. Yang, Y. Zhang, N. M. Nasrabadi, and T. S. Huang, "Close the loop: Joint blind image restoration and recognition with sparse representation prior." in ICCV, 2011.

[24] F. Sroubek and P. Milanfar, "Robust multichannel blind deconvolution via fast alternating minimization." in IEEE Trans. on Image Processing, pp. 16871700, 2012.

[25] X. Zhu, F. Sroubek, P. Milanfar, "Deconvolving PSFs for a better motion deblurring using multiple images." in ECCV, 2012.

[26] A. Levin, Y. Weiss, F. Durand, and W. T. Freeman. "Understanding and evaluating blind deconvolution algorithms." In IEEE Proceedings of International Conference on Computer Vision and Pattern Recognition (CVPR), pp. 19641971.

[27] Y. Hacohen, E. Shechtman, and D. Lischinski, "Deblurring by example using dense correspondence." In IEEE Proceedings of International Conference on Computer Vision (ICCV), pp. 23842391, 2013.

[28] J. Pan, Z. Hu, Z. Su, and M. H. Yang, "Deblurring face images with exemplars." In Proceedings of European Conference on Computer Vision (ECCV), pp. 4762. Springer, 2014.

[29] W.S. Lai, J. B. Huang, Z. Hu, N. Ahuja, and M. H. Yang, "A comparative

study for single image blind deblurring." In IEEE Proceedings of International Conference on Computer Vision and Pattern Recognition (CVPR). IEEE, 2016.

[30] A. Chakrabarti, "A neural approach to blind motion deblurring." In Proceedings of European Conference on Computer Vision (ECCV), pp. 221235. Springer, 2016.

[31] M. Hradis, J. Kotera, P. Zemck, and F. Sroubek, "Convolutional neural networks for direct text deblurring." In Proceedings of British Machine Vision Conference (BMVC), 2015.

[32] J. Sun, W. Cao, Z. Xu, and J. Ponce, "Learning a convolutional neural network for non-uniform motion blur removal." In IEEE Proceedings of International Conference on Computer Vision and Pattern Recognition (CVPR), pp. 769777, 2015.

[33] S. S. Sancevero, A. Z. Remacre, R. S. Portugal, "O papel da inverso para a impedncia no processo de caracterizao ssmica de reservatrios." in Revista Brasileira de Geofsica, p. 495-512, v. 24, 2006.

[34] P. J. Harvey, and D. J. MacDONALD, "Seismic modelling of porosity within the jurassic aged carbonate bank, offshore Nova Scotia," in Canadian Journal of Exploration Geophysics, num. 26, pp. 5471.

[35] G. Mavko, T. Mukerji, and J. Dvorkin, "The Rock Physics Handbook: Tools for Seismic Analysis of Porous Media." Cambridge: Cambridge University Press, pp. 359-369, 2009.

[36] H. DEBEYE, and P. RIEL van, "Lp-norm deconvolution." 1990, Geophysical Prospecting, pp. 381403

[37] S. Chopra, "Integrating coherence cube imaging and seismic inversion." The Leading Edge, pp. 354362, 2001.

[38] R. Dahl, M. Norouzi, and J. Shlens, "Pixel recursive super resolution" CoRR, 2017.

[39] V. Nair, and G. E. Hinton. "Rectified linear units improve restricted boltzmann machines." In Proc. 27th International Conference on Machine Learning, 2010.

[40] N. Qian, "On the momentum term in gradient descent learning algorithms," in Neural Networks, vol. 12, pp. 145-151, 1999.

[41] S. Narayana, and P. K. Thirivikraman, "Image similarity using fourier transform," in International Journal of Computer Engeneering and Technology, 2015, num. 6, pp. 2937.